Electronic supporting information:
Solid wetting-layers at inorganic nano-reactors: the water at imogolite nanotubes case

Geoffrey Monet[1], Erwan Paineau[1], Ziwei Chai[2], Mohamed S. Amara[1], Andrea Orecchini[3], Mónica Jimenéz-Ruiz[4], Alicia Ruiz-Caridad[1,4], Lucas Fine[4], Stéphan Rouzière[1], Li-Min Liu[2,5], Gilberto Teobaldi[2,6,7,8], Stéphane Rols[4], and Pascale Launois[1]

[1]Laboratoire de Physique des Solides, CNRS, Université Paris-Sud, Université Paris-Saclay, 91405 Orsay Cedex, France
[2]Beijing Computational Science Research Centre, 100193 Beijing, China
[3]Dipartimento di Fisica e Geologia and CNR-IOM, Università di Perugia, Via Pascoli s.n.c, I-06123 Perugia, Italy
[4]Institut Laue-Langevin, BP 156, 38042 Grenoble, France
[5]School of Physics, Beihang University, 100191 Beijing, China
[6]Scientific Computing Department, STFC, Harwell Campus, OX11 0QX Didcot, UK
[7]Stephenson Institute for Renewable Energy, Department of Chemistry, University of Liverpool, L69 3BX Liverpool, UK
[8]School of Chemistry, University of Southampton, SO17 1BJ Southampton, UK

February 13, 2020

1 Thermogravimetric analysis

Thermogravimetric analysis (TGA) was performed with a TGA Q50 (V20.10 Build 36) apparatus. A mass of $\sim 20\,$mg of a powder of hydrated single-walled alumino-germanate nanotubes (SW Ge-INT, nominal formula $GeAl_2O_7H_4$) was heated under nitrogen gas flow with a temperature ramp of $10\,°$C/min. TG and DTG (Differential Thermogravimetric) curves are shown in figure 1. Below $200\,°$C, a two-step weight loss process is evidenced, with a pronounced DTG minimum at $70\,°$C followed by a second one at $130\,°$C. Complete dehydration is reached around $200\,°$C. The total weight loss represents $28\,\%$ of the nanotube weight. Weight loss at $100\,°$C is $20\,\%$. There is thus about $8\,\%$ in weight of water which is strongly bonded to the nanotube and which only desorbs above $100\,°$C. The mass ratio of a water molecule to the $GeAl_2O_7H_4$ entity forming the nanotube wall being equal to 0.074, one concludes that there is one bonded water molecule per $GeAl_2O_7H_4$ entity.
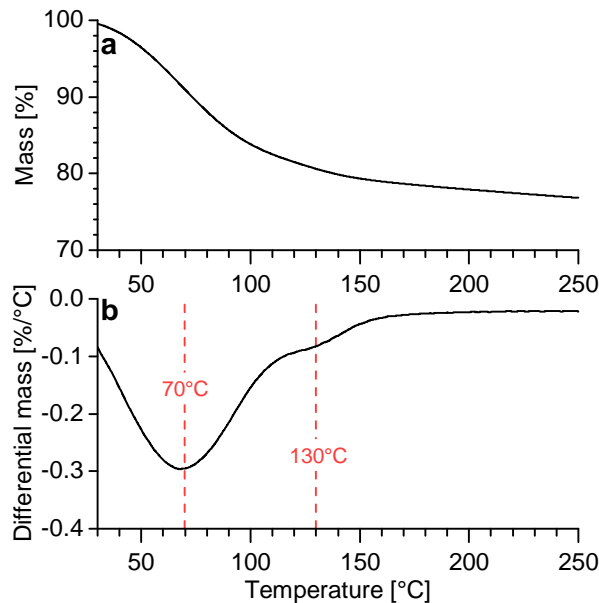

Figure 1: a: thermo-gravimetric curve measured on a powder of SW Ge-INTs; b: differential thermo-gravimetric (DTG) curve. Vertical dotted lines indicate DTG minima.

2 Determination of the nanotube chiral indices from Wide Angle X-Ray Scattering

Few milligrams of powder of single-walled alumino-germanate INTs were put in a sealed borosilicate capillary with a diameter of $0.7\,$mm. WAXS experiment was performed using a copper rotating anode generator and multilayer W/Si optics, providing a monochromatic beam with incident wavelength $\lambda = 1.5418\,$Å. The sample was put in a vacuum chamber to optimise the signal over background ratio. Scattered intensity was recorded on a large cylindrical image plate centred on the sample, with a radius of $104.8\,$mm. Pixels counts were angularly summed and intensity versus wave-vector

Q curves were thus obtained. Values as large as $8\,\text{Å}^{-1}$ are reached (figure 2). Intensity is corrected for polarisation and geometrical factors. Experimental resolution was determined using a reference quartz powder. It is a Gaussian function characterised by its full-width at half-maximum FWHM $0.024\,\text{Å}^{-1}$. Another experiment, using a molybdenium rotating anode generator and multilayer W/Si optics with a MAR research X-ray-sensitive plane detector behind the sample, allowed us to complement WAXS data at smaller Q-values (inset in figure 2).

We introduced in ref. [6] a fitting procedure to resolve the atomic structure of single walled nanotubes with complex stoichiometry from powder Wide Angle X-ray Scattering (WAXS) diagrams. It was successfully applied to methylated alumino-silicate and alumino-germanate nanotubes. We apply here this methodology to alumino-germanate imogolite nanotubes of nominal composition $GeAl_2O_7H_4$.

Following the convention adopted for single walled carbon nanotubes, the structure of an imogolite nanotube can be labeled by a pair of integers, which are the components of the so-called 'chiral vector'. The best agreement between simulated and experimental WAXS diagram is obtained for chiral indices (22,0) (see figure 2). As shown by ab initio molecular dynamic simulations, bonded water molecules inside the nanotubes form a highly ordered network (figure 2 (b)). The calculated XRS pattern of the nanotube with bound water inside is found to be very similar to that of the dry nanotube (see figure 2), as expected since the additional water molecules are not the major component of the electronic density of the system. This justifies that the structural refinement was carried out assuming a dry nanotube.

Calculations were performed for a powder of individual nanotubes [6]. Inset in figure 2 displays large oscillations characteristic of the squared form factor of single-walled nanotubes without any positional ordering. If the nanotubes were organised in bundles on a bidimensional lattice, peaks characteristic of the reciprocal lattice would have been observed [1, 7]. It can therefore be concluded that nanotubes are *not* organised in bundles so that the powder is formed of individual nanotubes.
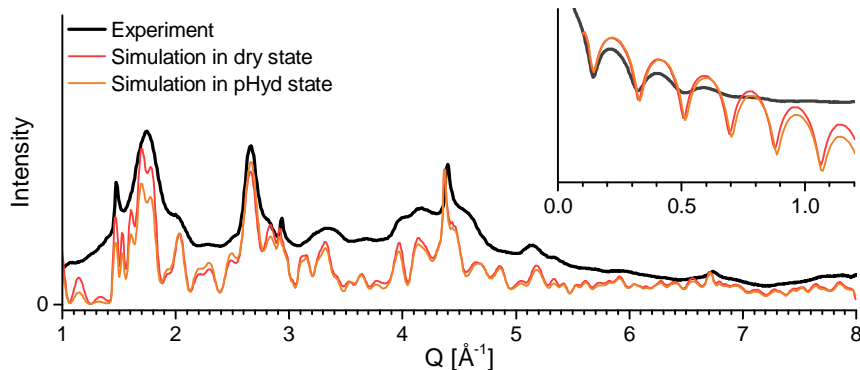

Figure 2: Comparison between experimental and calculated WAXS diagrams for a powder of dry single-walled aluminogermanate INTs. Calculations were performed for nanotubes with an internal radius of $14.3\,\text{Å}$, an external radius of $18.8\,\text{Å}$, an axial period of $8.64\,\text{Å}$ and a length of $450\,\text{Å}$, in agreement with ref. [2]. They were further convoluted to the experimental resolution. Calculations performed for partially hydrated (pHyd) INTs are also shown for comparison. The intensity in the inset is displayed in log scale.

3   Supplementary Density Functional Theory methods

DFT simulations were performed with the CP2K/Quickstep package [11] using the Perdew-Burke-Ernzerhof (PBE [8]) approximation to the exchange and correlation functional. Core electrons were described with norm-conserving Goedecker, Teter, and Hutter (GTH) pseudopotentials [4]. Valence electron Kohn-Sham states were expanded in terms of Gaussian functions with molecularly optimised double-ζ polarised basis sets (m-DZVP), tested to lead to small basis set superposition errors [10]. The auxiliary plane-wave basis set was expanded up to $320\,\text{Ry}$. Reciprocal space sampling was restricted to the Γ point. The adopted convergence thresholds for geometry optimisation were $10^{-4}\,\text{HaBohr}^{-1}$ on the maximum atomic force, and $3 \times 10^{-4}\,\text{HaBohr}^{-1}$ on the root mean square residual of all the atomic forces. Calculations were performed using periodic boundary conditions with $> 20\,\text{Å}$ vacuum-buffer perpendicularly to the nanotube axis. The (PBE) optimised nanotube period was $8.48\,\text{Å}$.

Adsorption energies (E_{ads}) were computed as the difference between the energy of the optimised pHyd Ge-INT ($E_{pHyd\ Ge-INT}$), the energy of the *isolated* optimised dry Ge-INT (E_{Ge-INT}), and the energy of one optimised H_2O molecule (E_{H_2O}), with the result normalised to the number n of H_2O molecules in the system ($n = 44$):

$$E_{ads} = \frac{(E_{pHyd\ Ge-INT} - E_{Ge-INT} - nE_{H_2O})}{n} \tag{1}$$

I_h ice was modelled in a ($9.05 \times 14.76 \times 15.66\,\text{Å}^{-3}$) orthorhombic cell containing $m = 64\ H_2O$ molecules and set up based on a $0.917\,\text{grcm}^{-3}$ density. The cohesive energy for hexagonal (I_h) ice (E_{coh}) was calculated as the difference between the energy of the optimised I_h ice box (E_{I_h}) and that of one optimised H_2O molecule (E_{H_2O}), with the result normalised to the number m of H_2O molecules in the system ($m = 64$):

$$E_{coh} = \frac{(E_{I_h} - mE_{H_2O})}{m} \tag{2}$$

Eq. (S2) was also used to calculate the cohesive energy for the reference H_2O cylindrical bilayer (BL, see Figure S12), accounting for the change in the number of H_2O molecules in the system (m=88).

Both E_{ads} and E_{coh} quantify the interaction energy experienced by the molecules in the solid by subtracting the energy of the optimised constituents to the energy of the composite. Thus, in spite of the different labeling, E_{ads} and E_{coh} are conceptually equivalent, which enables meaningful comparison of these two quantities.

Vibrational zero-point energies (ZPE) were calculated on the basis of the harmonic internal vibrational normal modes, of wavenumber ω_i ($i = 1 - 3$), computed by finite displacements for one selected H_2O molecule in the wetting-layer and I_h ice simulation cell:

$$ZPE = \frac{\hbar}{2} \sum_{i=1}^{3} \omega_i \tag{3}$$

Canonical (NVT) Molecular dynamic (MD) simulations were propagated on fully hydrogenated models (namely, a nanotube with nominal composition $GeAl_2O_7H_4$ and a partially hydrated one with one water molecule per germanium atom) for over $23\,\text{ps}$ with a time step of $0.5\,\text{fs}$. The NVT-MD simulations were thermostated at $T = 150\,\text{K}$ via a Nose-Hoover chain [5] of length 4 and $50\,\text{fs}$ time-constant (massive thermostat region CP2K option), tested to yield homogeneous thermalisation of the nanotube, inclusive of the peripheral hydroxyl groups.

4 Atomic density maps

DFT-MD simulations at 150 K are used to calculate atomic density maps (excluding the first 3 ps of simulation). Figures 3 and 4 show the probability density of the atoms projected on the Oxy plane perpendicular to the Oz axis of the nanotube. Atomic density maps are generated by dividing projection surfaces into squares with 0.1 Å side. Low frequency contributions with large amplitude motion induce a blurring of atomic density maps. For improved readability, we apply a rectangular high-pass filter with a 2 meV cut-off, while keeping the 0 meV contribution (mean atomic density), see figure 3. The same procedure was applied to figures 2 (a) and (b).
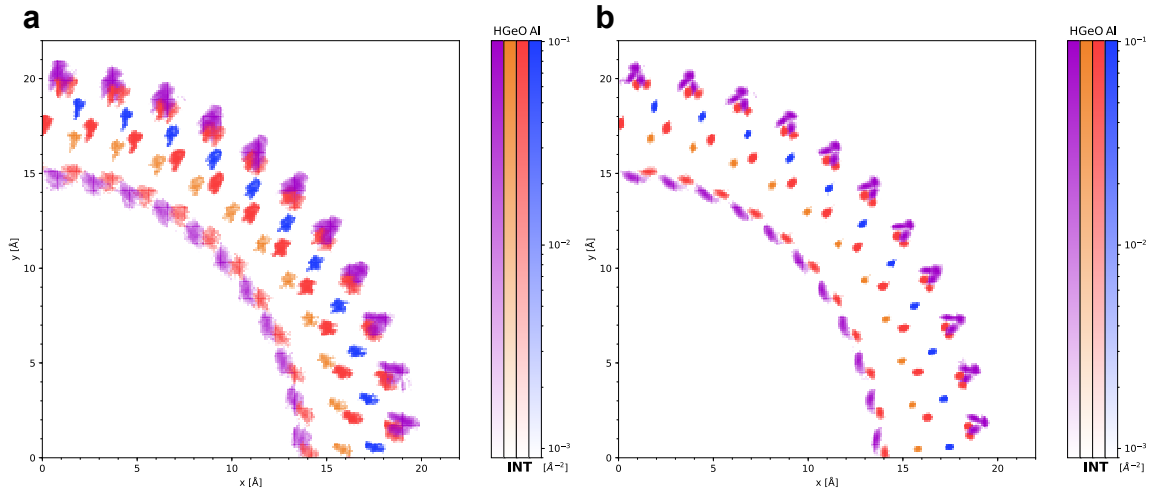

Figure 3: colour map displaying the probability density of an aluminum atom (in navy blue), germanium (in orange), oxygen (in red) and hydrogen (in purple) expressed in Å^{-2}. The map on the left (a) results from the raw trajectories of the atoms of the dry INT, the one on the right (b) is obtained from the same trajectory after the application of a 2 meV high-pass filter.
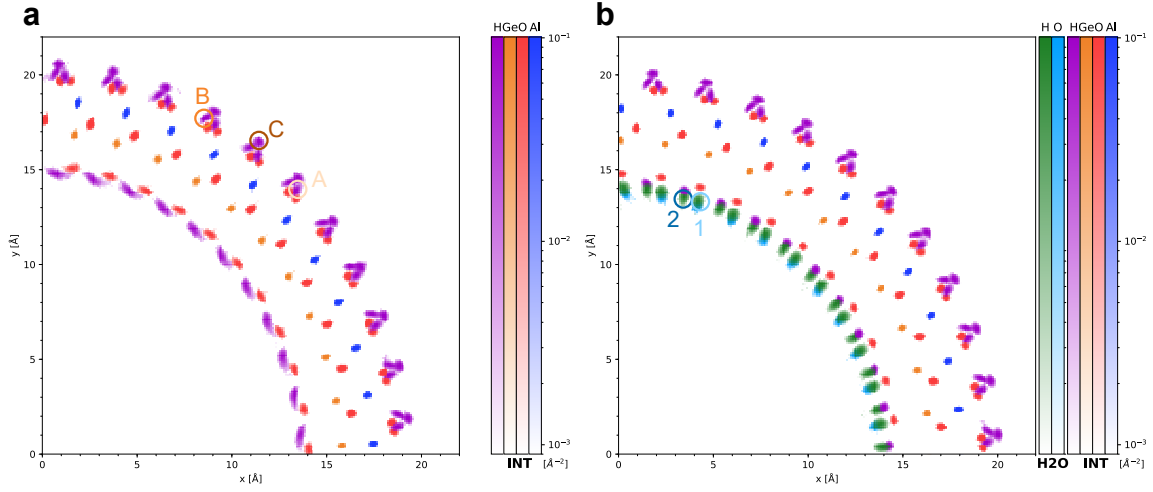
Figure 4: Atomic density colour map for (a) dry INT and (b) partially hydrated INT with a water to germanium ratio equal to one, once a 2 meV high-pass filter is applied. The hydrogen and oxygen atoms of the water molecules are displayed with a different colour (green and light blue) to distinguish them from those of the nanotube.

5 Generalised density of state from Velocity Autocorrelation Functions

Vibrational density of states (DOS) of the different types of hydrogen atom (H_{H2O}: H atoms from water molecules - H_{in}: H atoms on INT inner wall - H_{out}: H atoms on INT outer wall) have been calculated from the velocity autocorrelation function (VACF)[3] deduced from DFT-MD trajectories at 150 K (the first three ps of the simulation were excluded). The vibrational densities of state of the different hydrogen populations are reported in figure 5 for dry nanotubes and figure 6 for hydrated ones.

To calculate GDOS from vibrational densities of state and allow direct comparison with inelastic neutron scattering measurement, multiphonon corrections have been computed [9] and DOS have been convoluted to the experimental resolution. The experimental resolution in energy is a Gaussian function characterised by its Full Width at Half Maximum (FWHM). FWHM is taken equal to 1.5 meV, 6 meV and 3 % of incident energy for, respectively, 1.7 Å IN4C, 0.9 Å IN4C and IN1 part of generalised density of state.

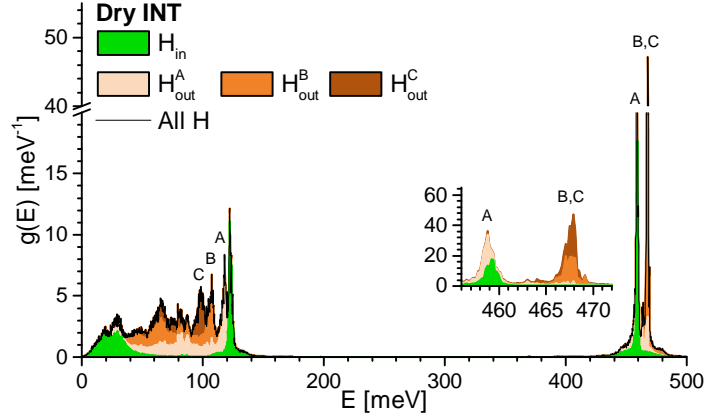Figure 5: Vibrational density of state of the dry nanotube (black line). The contributions of the different hydrogen populations (H_{in} for H atoms on the inner wall of the nanotube, H_{in}^A, H_{in}^B and H_{in}^C for the three types of H atoms outside the nanotube (see figure 4)) are represented by coloured stacked-areas. The inset is a zoom on the stretching modes.
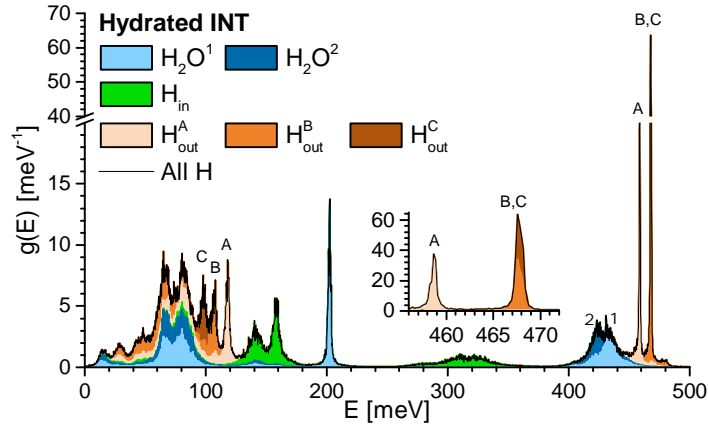

Figure 6: Vibrational density of state of the pHyd nanotube (black line). The contributions of the different hydrogen populations (H_{in} for H atoms on the inner wall of the nanotube, H_{in}^A, H_{in}^B and H_{in}^C for the three types of H atoms outside the nanotube, H_2O^1 and H_2O^2 for the hydrogen atoms of a water molecule (see figure 4)) are represented by coloured stacked-areas. The inset is a zoom on the stretching modes.

6 Trajectory spectral filtering

We compute the Fourier transforms of the trajectories of all atoms at $150\,\mathrm{K}$ and we apply a rectangular bandpass filter on the energy range of interest, keeping the zero energy component which corresponds to average positions. Inverse Fourier transform is then applied to the filtered Fourier transforms so that one finally obtains trajectories corresponding only to the frequency range of

7

interest.

The videos and images in figures 7-10 of the filtered trajectories were produced using the tri-dimensional computer graphics software Blender. Corresponding videos are available at the following link: gmonet.github.io/papers/CS2020.

Hydrogen and oxygen atoms are represented by light pink and red spheres, respectively. AlO_6 octahedra and GeO_4 tetrahedra are shown in blue and in green. Movies are recorded at 60 frames per second. The time step of the molecular simulation being 0.5 fs, one second of video corresponds to 30 fs of the simulation. The duration of a video is 30 seconds corresponding to 1 ps of molecular simulation. Black traces correspond to the trace left by H and O atoms during their displacements. The size of this trace was multiplied by a factor s chosen according to the amplitude of the vibration in order to highlight small magnitude motions. Dark-blue arrows are drawn to help visualise the vibrational motions. The red, green and blue arrows on the lower-left corner correspond respectively to the x, y and z axes of an orthonormal basis, where z-axis is the long axis of the tube.

The vibrational density of states of external hydrogen atoms is roughly independent of the presence of water inside the nanotube (see figures 5 and 6). In figure 7, the bending and stretching motions of the three types of external hydrogen atoms A, B and C -identified on atomic density maps in figure 4- are thus shown only for the dry nanotube.
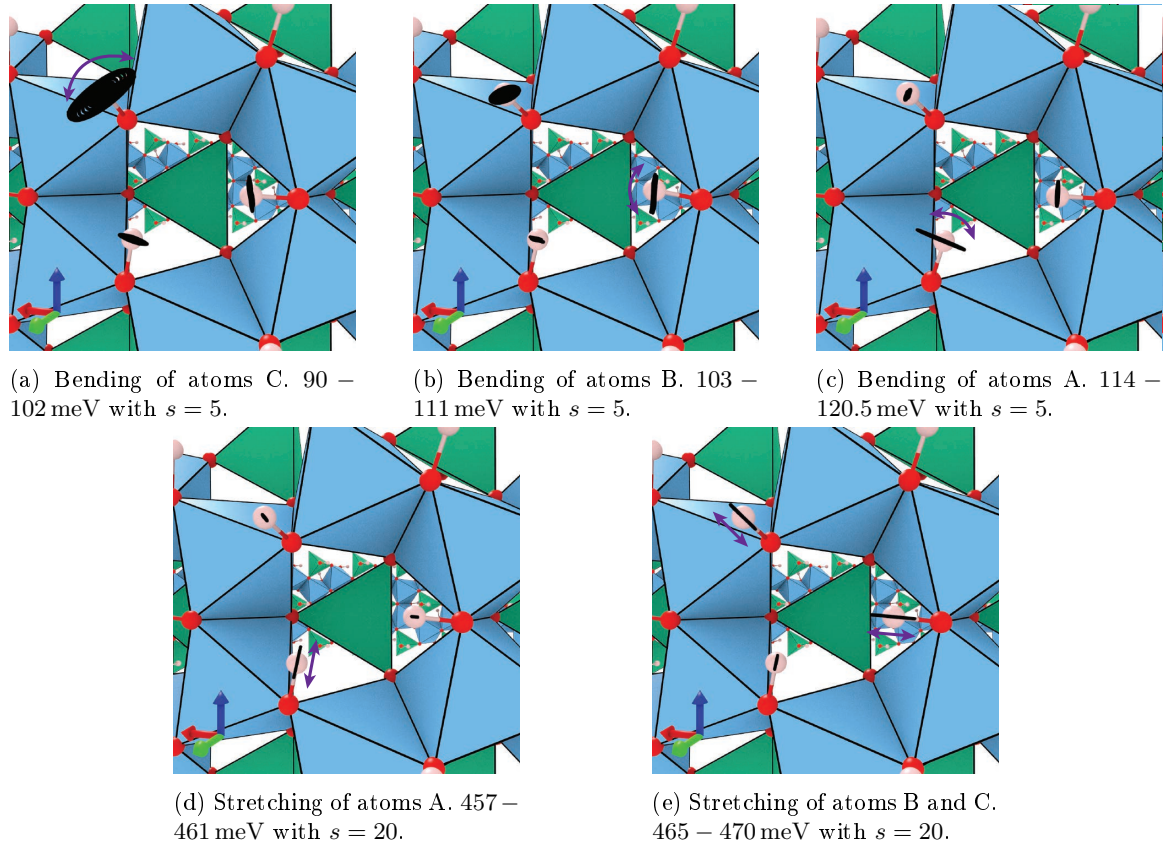

(a) Bending of atoms C. $90 - 102$ meV with $s = 5$.

(b) Bending of atoms B. $103 - 111$ meV with $s = 5$.

(c) Bending of atoms A. $114 - 120.5$ meV with $s = 5$.

(d) Stretching of atoms A. $457 - 461$ meV with $s = 20$.

(e) Stretching of atoms B and C. $465 - 470$ meV with $s = 20$.

Figure 7: H_{out} motions in dry INT.

Figures 8 and 9 show the vibration modes of the inner hydrogen (H_{in}) for dry and pHyd nan-

otubes. Subfigures (a) illustrate the significant alteration of the twisting motion in the presence of water molecules.
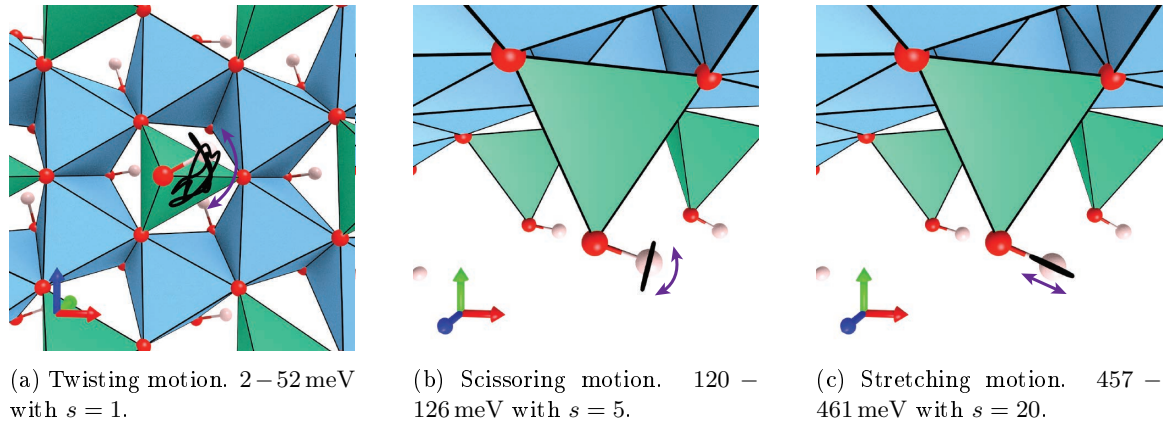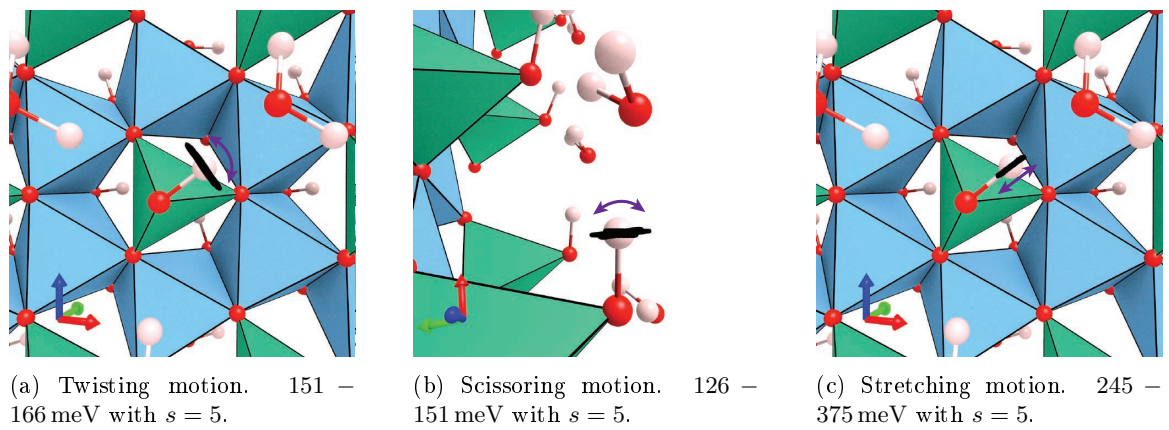

(a) Twisting motion. $2-52$ meV with $s = 1$.

(b) Scissoring motion. $120 - 126$ meV with $s = 5$.

(c) Stretching motion. $457 - 461$ meV with $s = 20$.

Figure 8: H_{in} motions in dry INT.

(a) Twisting motion. $151 - 166$ meV with $s = 5$.

(b) Scissoring motion. $126 - 151$ meV with $s = 5$.

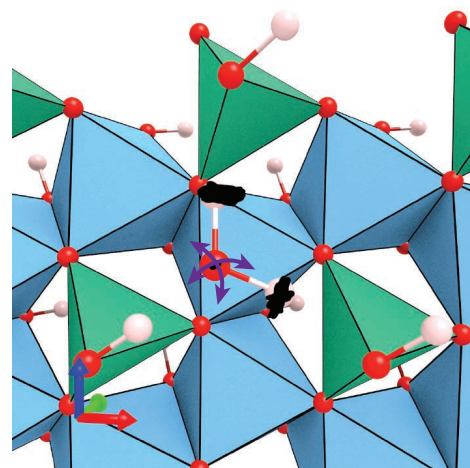(c) Stretching motion. $245 - 375$ meV with $s = 5$.
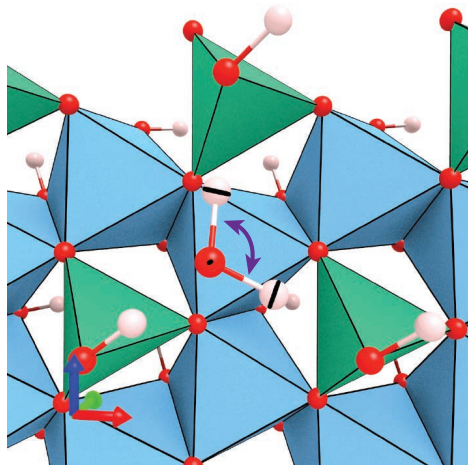
Figure 9: H_{in} motions in hydrated INT.

Figure 10 shows the vibration modes of the water molecules inside the nanotube, corresponding to a translation mode, the libration band, a bending mode and two stretching modes.
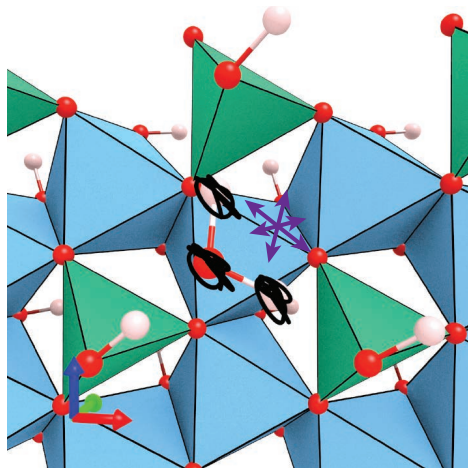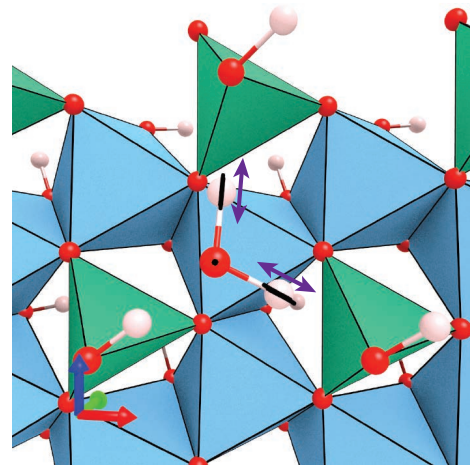
(a) Translation motion. $8 - 22\,\text{meV}$ with $s = 2$.

(b) Libration motions. $55 - 100\,\text{meV}$ with $s = 2$.

(c) Bending motion. $196 - 210\,\text{meV}$ with $s = 5$.

(d) Stretching motions. $400 - 452\,\text{meV}$ with $s = 5$.

Figure 10: H$_2$O motions in hydrated INT.
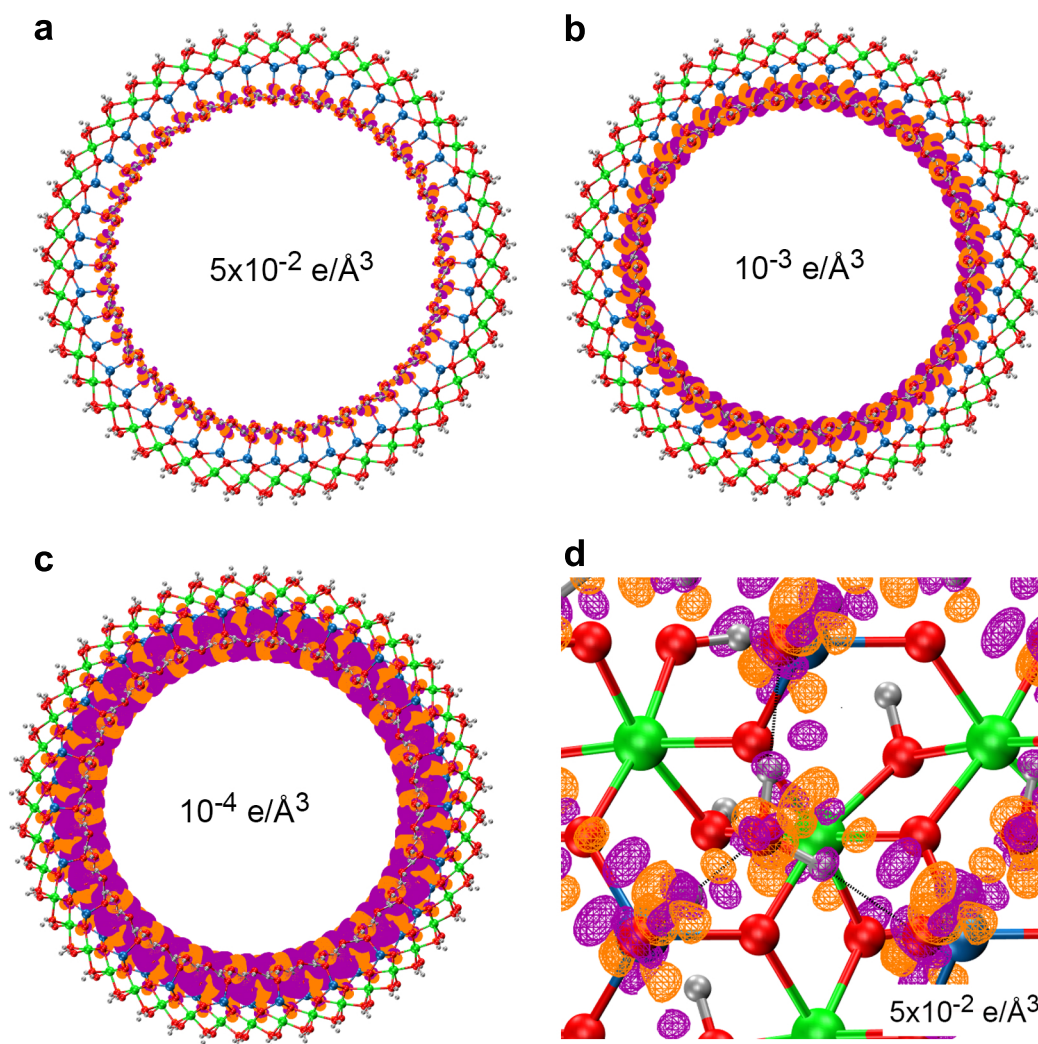
7 Supplementary Density Functional Theory Results

Figure 11: Front view (a-c) and side close up (d) of the calculated electronic density change (DFT, $T = OK$), $\Delta\rho$, due to Ge-INT/H_2O re-hybridisation. $\Delta\rho = \rho(pHydGe - INT) - \rho(Ge - INT) - \rho(H_2O)$. Orange: $\Delta\rho > 0$, purple: $\Delta\rho < 0$. The value of the displayed iso-contour is reported on each panel.
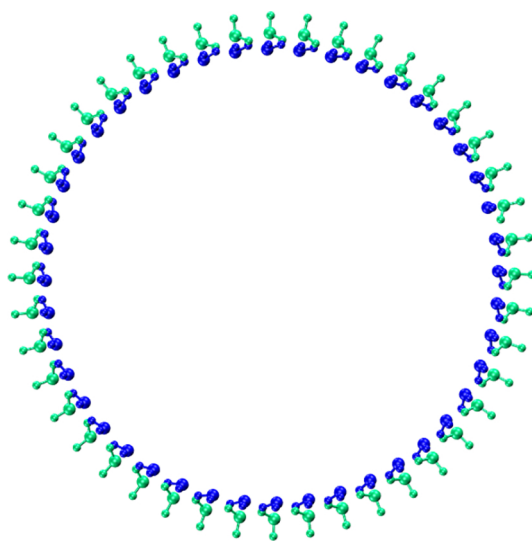
Figure 12: Front view of the reference H_2O cylindrical bilayer (BL). All the atomic positions are the same as for the optimised pHyd Ge-INT system apart from the outermost H-atoms. The outermost H-atoms lie along the same direction as the Ge−O bonds in the pHyd Ge-INT, with a $1.049\,\text{Å}$ distance from the closest O-atoms (as for the O-H_{in} bonds in the pHyd Ge-INT).

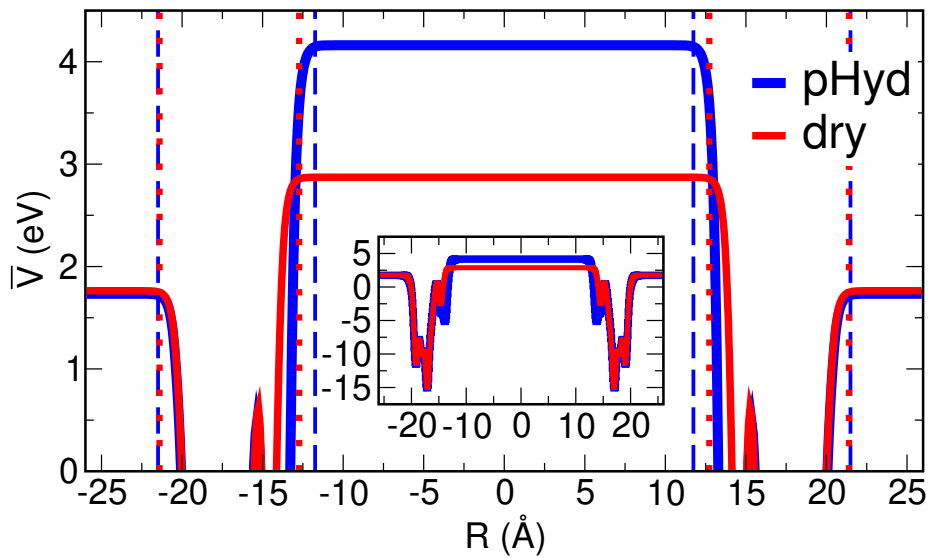Figure 13: Average electrostatic potential $\overline{V}$ along the nanotube's radius R for the pHyd and the dry Ge-INT (DFT, $T = 0\,\mathrm{K}$). The dashed (dotted) vertical lines mark the onset of the vacuum electrostatic plateaus, defined on the basis of a $0.005\,\mathrm{eV}$ threshold on the potential oscillations [6]. As evident from the vacuum-plateus, and owing to the cylindrical symmetry, no electrostatic field is present inside or outside the nanotube cavity.

References

[1]   Mohamed Salah Amara et al. "Hexagonalization of Aluminogermanate Imogolite Nanotubes Organized into Closed-Packed Bundles". In: *The Journal of Physical Chemistry C* 118.17 (May 2014), pp. 9299–9306. ISSN: 1932-7447, 1932-7455. DOI: 10.1021/jp5029678.

[2]   Mohamed Salah Amara et al. "Hybrid, Tunable-Diameter, Metal Oxide Nanotubes for Trapping of Organic Molecules". en. In: *Chemistry of Materials* 27.5 (Mar. 2015), pp. 1488–1494. ISSN: 0897-4756, 1520-5002. DOI: 10.1021/cm503428q.

[3]   J. M. Dickey and Arthur Paskin. "Computer Simulation of the Lattice Dynamics of Solids". en. In: *Physical Review* 188.3 (Dec. 1969), pp. 1407–1418. ISSN: 0031-899X. DOI: 10.1103/PhysRev.188.1407.

[4]   S. Goedecker, M. Teter, and J. Hutter. "Separable Dual-Space Gaussian Pseudopotentials". en. In: *Physical Review B* 54.3 (July 1996), pp. 1703–1710. ISSN: 0163-1829, 1095-3795. DOI: 10.1103/PhysRevB.54.1703.

[5]   Glenn J. Martyna, Michael L. Klein, and Mark Tuckerman. "Nosé–Hoover Chains: The Canonical Ensemble via Continuous Dynamics". en. In: *The Journal of Chemical Physics* 97.4 (Aug. 1992), pp. 2635–2643. ISSN: 0021-9606, 1089-7690. DOI: 10.1063/1.463940.

[6]   Geoffrey Monet et al. "Structural Resolution of Inorganic Nanotubes with Complex Stoichiometry". en. In: *Nature Communications* 9.1 (Dec. 2018), p. 2033. ISSN: 2041-1723. DOI: 10.1038/s41467-018-04360-z.

[7]   Erwan Paineau et al. "Effect of Ionic Strength on the Bundling of Metal Oxide Imogolite Nanotubes". en. In: *The Journal of Physical Chemistry C* 121.39 (Oct. 2017), pp. 21740–21749. ISSN: 1932-7447, 1932-7455. DOI: 10.1021/acs.jpcc.7b07391.

[8]   John P. Perdew, Kieron Burke, and Matthias Ernzerhof. "Generalized Gradient Approximation Made Simple". en. In: *Physical Review Letters* 77.18 (Oct. 1996), pp. 3865–3868. ISSN: 0031-9007, 1079-7114. DOI: 10.1103/PhysRevLett.77.3865.

[9]   Helmut Schober. "An Introduction to the Theory of Nuclear Neutron Scattering in Condensed Matter". In: *Journal of Neutron Research* 17.3-4 (2014), pp. 109–357. ISSN: 1023-8166. DOI: 10.3233/JNR-140016.

[10] Joost VandeVondele and Jürg Hutter. "Gaussian Basis Sets for Accurate Calculations on Molecular Systems in Gas and Condensed Phases". en. In: *The Journal of Chemical Physics* 127.11 (Sept. 2007), p. 114105. ISSN: 0021-9606, 1089-7690. DOI: 10.1063/1.2770708.

[11] Joost VandeVondele et al. "Quickstep: Fast and Accurate Density Functional Calculations Using a Mixed Gaussian and Plane Waves Approach". en. In: *Computer Physics Communications* 167.2 (Apr. 2005), pp. 103–128. ISSN: 00104655. DOI: 10.1016/j.cpc.2004.12.014.